3D geometry and displacement transfer of an oblique relay zone on outcropping normal faults

Giovanni Camanni [a,b,*], Giovanni Freda [a,c], Efstratios Delogkos [b], Andrew Nicol [d], Conrad Childs [b,e]

[a] DiSTAR, Università degli Studi di Napoli "Federico II", Naples, Italy
[b] Fault Analysis Group, UCD School of Earth Sciences, University College Dublin, Belfield, Dublin 4, Ireland
[c] Dipartimento di Scienze Chimiche e Geologiche, Università di Modena e Reggio Emilia, Modena, Italy
[d] School of Earth and Environment, University of Canterbury, Christchurch, 8140, New Zealand
[e] Irish Centre for Research in Applied Geosciences (iCRAG), UCD School of Earth Sciences, University College Dublin, Belfield, Dublin 4, Ireland

A B S T R A C T

Relay zones on normal faults accommodate transfer of displacement between adjacent fault segments. We study vertical and horizontal displacement transfer mechanisms across a relay zone adjacent to the Moab Fault at Courthouse Rock (Utah, USA). The relay zone has a reservoir scale (map overlap length ca. 750 m, separation ca. 150 m), and is bounded by two normal fault segments with maximum throw of ca. 12 m. The relay zone is exposed on multiple, sub-parallel cliff faces and intervening rock pavements. We use photogrammetry of these exposures to build a 3D virtual outcrop model of the relay-bounding faults, subordinate faults deforming the relay zone and seven faulted stratigraphic horizons. The relay-bounding faults are right-stepping in map view and contractional in cross-section, defining a relay zone oblique to bedding in 3D. Displacement is transferred both horizontally and vertically across the relay zone. Horizontal transfer of displacement is achieved by a shallow dipping ($<1°$) relay ramp, whereas vertical transfer is achieved by antithetic faults within the relay ramp. Our analysis demonstrates that multiple mechanisms can work in conjunction to facilitate transfer of displacement across individual relay zones.

1. Introduction

Normal faults are rarely simple planar surfaces and generally comprise several, synthetic fault segments between which displacement is transferred (Walsh and Watterson, 1989; Childs et al., 1996, 2009; Peacock, 2002; Marchal et al., 2003; Walsh et al., 2003; Kristensen et al., 2008; Delogkos et al., 2017; Camanni et al., 2021). Transfer of displacement between two fault segments is accommodated by deformation of the intervening rock volume, referred as a "relay zone" (Peacock and Sanderson, 1991, 1994; Childs et al., 1995; Huggins et al., 1995; Camanni et al., 2019, 2023; Delogkos et al., 2020; Nicol et al., 2020; Roche et al., 2020, 2021). Relay zones are generally recognised from 2D sections through them, either in map view or subvertical cross section. The faults that bound relay zones observed in map view are separated by a volume of rock that is often rotated about an axis normal to fault strike; in horizontally-bedded rocks this rotation is seen as a panel of steepened bedding, referred to as a relay ramp (Fig. 1A). These

map view relay zones are commonly referred to as lateral, strike or neutral relay zones (Peacock and Sanderson, 1991, 1994; Cartwright et al., 1996; Crider and Pollard, 1998; Peacock, 2002; Fossen and Rotevatn, 2016; Camanni et al., 2019; Mercuri et al., 2020a, 2020b). In cross-section, adjacent synthetic fault segments may step across 'dip' relay zones (*sensu* Camanni et al., 2019). Depending on the sense of step of the segments, dip relay zones may be sites of contractional or extensional volumetric strains that can be accommodated in a variety of ways including rock volume change, minor faulting, open fracturing, and pressure solution (Peacock and Zhang 1993; Childs et al., 1996; Rykkelid and Fossen, 2002; van der Zee and Urai, 2005; Kristensen et al., 2008; Putz-Perrier and Sanderson, 2008; Ferrill et al., 2014; Camanni et al., 2019, Fig. 1B). It has recently been shown that displacement transfer across dip relay zones can be achieved through antithetic faults that carry displacement between the relay zone-bounding faults (Camanni et al., 2023, and references therein; Fig. 1C).

Neutral and dip relay zones are end-members in a spectrum with
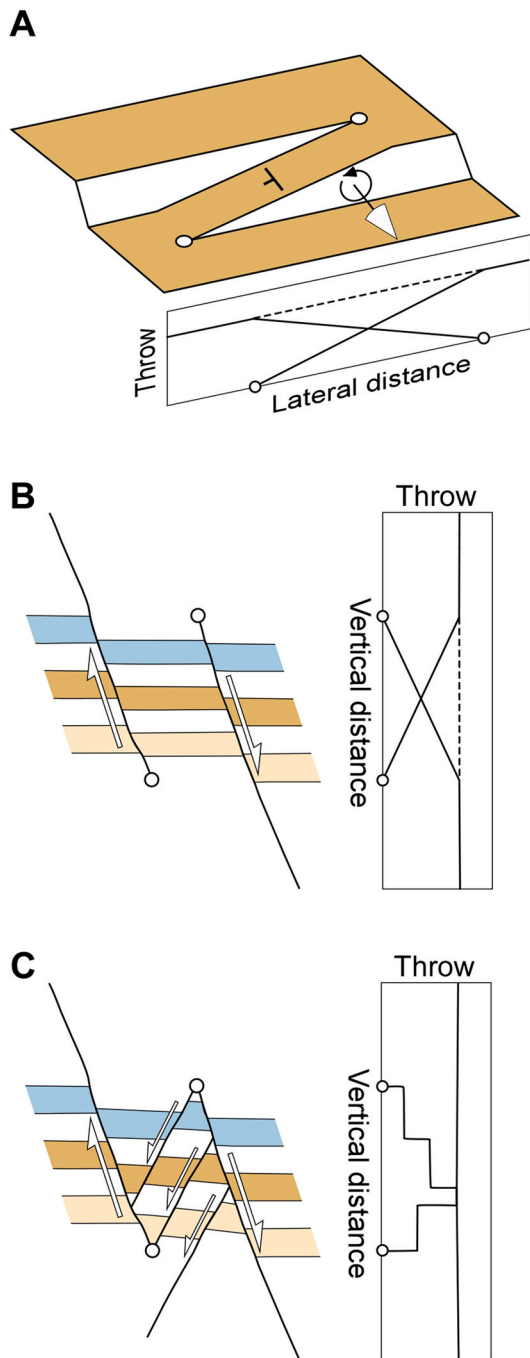
A

B

C

Fig. 1. Mechanisms for achieving horizontal (**A**) and vertical (**B, C**) displacement transfer across, respectively, neutral and dip relay zones (*sensu* Camanni et al., 2019) on normal faults, and associated throw profiles. **A**: relay ramp; **B**: volumetric change (contractional, in this example); **C**: antithetic faulting (see Camanni et al., 2023). References to these three modes of displacement transfer can be found in the main text.

intermediate geometries referred to as 'oblique' relay zones (e.g., Camanni et al., 2019; Roche et al., 2021). However, oblique relay zones are rarely identified as this requires 3D data. In a recent study using several high-resolution 3D seismic reflection surveys, Camanni et al. (2019) found that, while neutral and dip relays predominate, oblique relay zones are also common. However, seismic reflection data typically do not provide the resolution required to examine the internal structure of relay zones and there are no published accounts of the internal 3D structure of oblique relay zones. Here we provide an example of an oblique relay zone that can be mapped in 3D from outcrop allowing both

its geometry, the displacement distribution on the relay zone bounding faults, and the internal structure of the relay zone to be examined.

The structure studied is a reservoir-scale (map overlap length ca. 750 m, separation ca. 150 m) relay zone bounded by two normal faults, which each have a maximum throw of ca. 12 m and intersect the principal strand of the Moab Fault at Courthouse Rock (Utah, USA; Fig. 2). The relay zone occurs in a unique topographic setting in which two canyons approximately perpendicular to the strike of the faults, expose their traces on five consecutive, subparallel, ca. 100 m high, cliff faces and on the rock pavements between the faces. Therefore, the outcrop provides a unique opportunity to observe faults in both cross-section and map views, and most importantly to estimate throw variations in both horizontal and vertical directions along the faults at the high resolution provided by field data. These data are used to study in detail the geometry of the relay zone and the mechanisms that facilitate the transfer of displacement between the bounding faults.

2. Geology and 3D exposure of the studied outcrop

The study area is located in SE Utah (USA), about 30 km northwest of the town of Moab, within the intracratonic, Paradox Basin on the Colorado Plateau (Foxford et al., 1996, Fig. 2A). Subsidence of the Paradox Basin commenced as early as in the Proterozoic, but was largest in the mid Pennsylvanian, when it was associated with the deposition of ca. 1.8 km thick evaporites of the Paradox formation (Doelling, 2001; Nuccio and Condon, 1996; Stokes, 1987). Importantly for this paper, since their deposition these evaporites were deformed by several events of salt diapirism that occurred until the Late Tertiary and resulted in the development of salt-cored anticlines as well as normal faults near the hinge of the anticlines (Doelling, 1988, 2001; Foxford et al., 1996). This paper focuses on one of these normal faults, the Moab Fault (Fig. 2A and B; Foxford et al., 1996, 1998; Davatzes et al., 2005; van Gent and Urai, 2020), which was active, in association with salt remobilization, from the Triassic to the mid-Jurassic (Foxford et al., 1996, 1998) and again from the mid Cretaceous to the early Tertiary (Foxford et al., 1996, 1998; Doelling, 1988, 2001).

The Moab Fault is a northwest-striking, salt-related, normal fault, offsetting a Pennsylvanian to Cretaceous sequence mostly comprising sandstone, shale, and subordinate limestone (Fig. 2; McKnight, 1940; Doelling 1985, 1988, 2001; Foxford et al., 1996, 1998; Davatzes et al., 2003, 2005; Johansen et al., 2005; van Gent and Urai, 2020). The fault can be divided in two sections: a relatively simple southern section comprising a continuous, approximately straight fault (segment A in Fig. 2A), and a northern section which is composed of a series of west-stepping, hard-linked, fault splays (segments B, C, D, E in Fig. 2A; Foxford et al., 1996, 1998). Fault displacement is a maximum (ca. 960 m) along the southern section, and decreases northwards, towards and then across, the fault splays that make up the northern section (Foxford et al., 1996, Fig. 2C).

The relay zone studied here is located at Courthouse Rock, near the boundary between the southern and the northern sections of the Moab Fault (Fig. 2A; Davatzes et al., 2005; Johansen et al., 2005; van Gent and Urai, 2020; Camanni et al., 2023). Here, a series of approximately east-west striking normal faults intersect the northernmost part of segment A of the Moab Fault (Fig. 2A and 3; Davatzes et al., 2005; Johansen et al., 2005; van Gent and Urai, 2020; Camanni et al., 2023). Of these east-west faults, the two with the largest strike extent bound the relay zone studied in this work (Fig. 3). These faults dip to the north and displace a sequence of four major stratigraphic units that are Lower to Middle Jurassic in age (Fig. 2). From bottom to top of the sequence, these units are: the Navajo Sandstone Formation and the Dewey Bridge, Slick Rock, and Moab Tongue members of the Entrada Sandstone Formation (Figs. 2 and 4; Foxford et al., 1996, 1998; Maerten, 2000; Davatzes et al., 2003, 2005; Johansen et al., 2005; van Gent and Urai, 2020; Camanni et al., 2023). The Navajo Sandstone Formation, Slick Rock Member and Moab Tongue Member are sandstone-rich and mostly
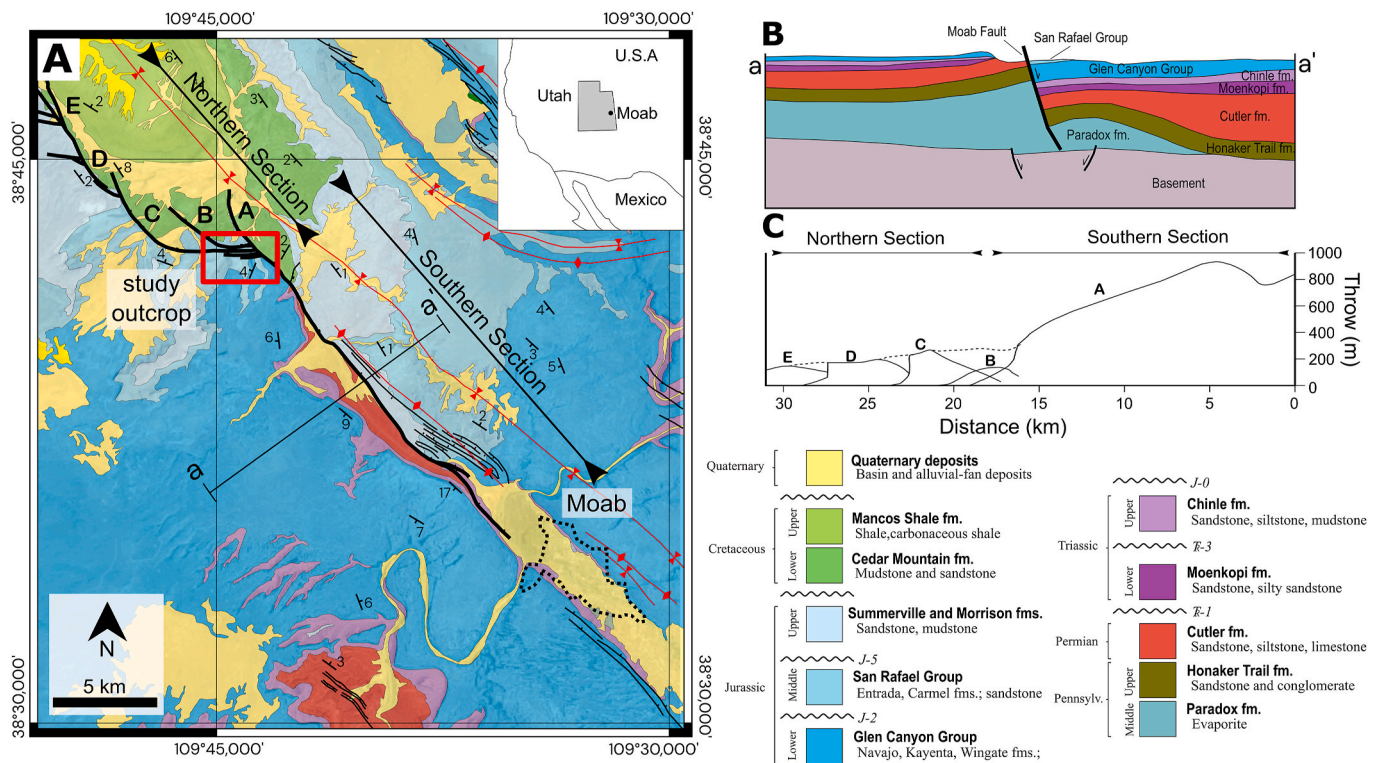
Fig. 2. A: Geology of the study area (modified after Doelling, 2001) and structure of the Moab Fault (modified after Foxford et al., 1996, 1998); note how the fault is subdivided in two sections and how the northern one is very segmented (segments B to E). The major unconformities indicated with wavy lines in the legend are from Pipiringos and O'Sullivan (1978); **B**: cross-section across the southern section of the Moab Fault (modified after Foxford et al., 1996, 1998); **C**: throw profile along the Moab Fault illustrating its northward decrease in throw (modified after Foxford et al., 1996, 1998). The red box in **A** indicates the location of Fig. 3. (For interpretation of the references to colour in this figure legend, the reader is referred to the Web version of this article.)
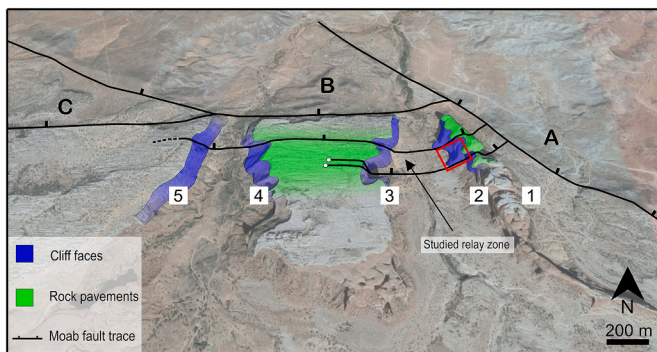

Fig. 3. 3D exposure and major faults of the study outcrop at Courthouse Rock. The cliff faces (1–5) along which the study faults crop out and the rock pavement between them are indicated in blue and green, respectively. The two ca. E-W faults south of segment B are the ones bounding the relay zone studied in this work. The red box indicates the location of Fig. 4. Location of this figure is indicated by the red box in Fig. 2. Background image from Google Earth. (For interpretation of the references to colour in this figure legend, the reader is referred to the Web version of this article.)

of aeolian origin, whereas the Dewey Bridge Member is a mixed sandstone-mudstone unit made up of sandstones fluvial and aeolian in origin, interbedded with floodplain/lacustrine mudstones and siltstones (Foxford et al., 1996, 1998).

At Courthouse Rock, the rock exposure is highly 3D and is associated with two canyons, which are 200–300 m wide and separate 100 m buttes. The canyons are oriented roughly north-south and the sub-vertical canyon walls provided multiple exposures of the same faults (Fig. 3; see also Camanni et al., 2023). The 100 m high canyon walls

(cliff faces, hereafter, and labelled 1 to 5 on Fig. 3) expose Dewey Bridge to Moab Tongue members of the Jurassic Entrada Sandstone Formation (Fig. 4). Rock pavements on the top of the buttes are developed within the Moab Tongue Member so that the faults can be mapped between the canyons (Fig. 3). The canyon floors are largely covered in sediments but provide partial exposure within the Dewey Bridge Member. At Court-house Rock bedding is shallow dipping (dip of ca. 4°–7°) to the NW and NNW, in the area between faces 1 and 2 and on the rock pavement be-tween faces 3 and 4, respectively (Fig. 5; see also Camanni et al., 2023).

3. Data and methods

We have developed a 3D model of the relay zone geometry and displacements using the cliff faces and rock pavements (Fig. 3). To produce the 3D model we first collected digital images in the field using an unmanned aerial vehicle (UAV, aka drone). These images, positioned by means of the UAV on-board GPS, were used to construct a 3D virtual outcrop model (VOM) of the exposure (see Supplementary Figs. 1, 2, 3). The VOM comprises a surface of $\sim 1.32 \times 10^6$ m^2, with a point cloud resolution of $\sim$59,2 point/m^2. Fault mapping and displacement analysis was carried out in 3D on the VOM and complemented by direct field observations. This methodological workflow is detailed below.

3.1. Fault and horizon characterisation

Horizons and the relay-bounding and subordinate faults were map-ped both in the field and on the VOM using Move software. Fault ori-entations were constrained by field measurements and by faults that outcrop on at least two adjacent cliff faces, or on one cliff face and an adjacent rock pavement. Horizons were readily correlated between the cliff faces allowing construction of 3D horizon surfaces and extraction of bedding orientations.
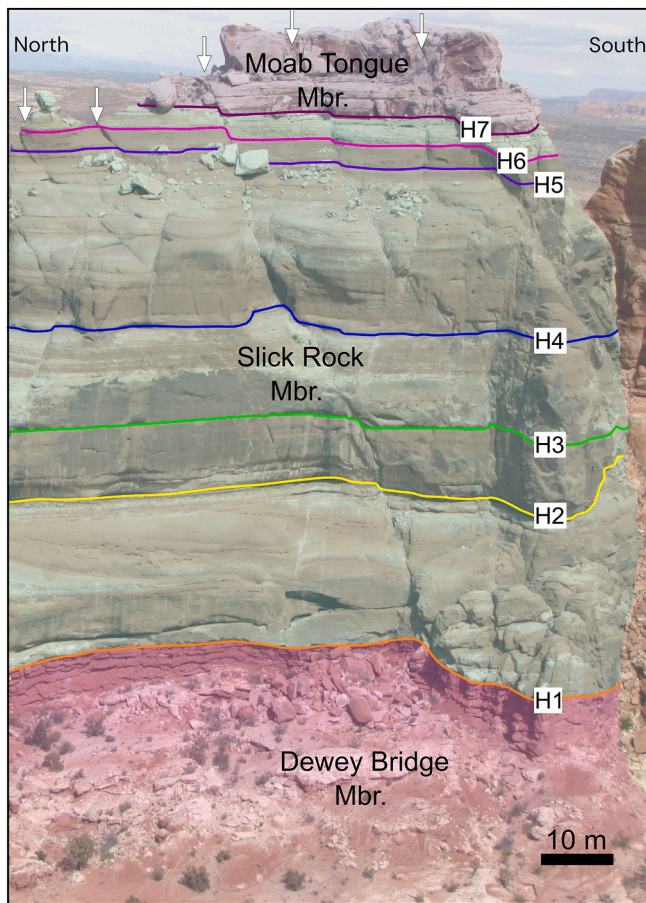
Fig. 4. Field photo of the entire vertical extent of the exposure on cliff Face 2. The horizons of the Entrada Sandstone Formation mapped throughout the study outcrop are marked. H1: top of the Dewey Bridge Member; H2 to H6: tens of cm thick mudstone layers within the Slick Rock Member; H7: top of the Slick Rock Member/base of the Moab Tongue Member. Approximate location of this figure is indicated by the red box in Fig. 3. Note that faults are not interpreted in this figure, but only arrowed at the top of the cliff. (For interpretation of the references to colour in this figure legend, the reader is referred to the Web version of this article.)

Seven horizons (named, from bottom to top, H1 to H7) were mapped and used for detailed fault throw measurements and for estimates of bed dips in the relay zone (Fig. 4). Although the Entrada Sandstone Formation includes several internal angular unconformities resulting in variations in layer thickness (e.g., Pipiringos and O'Sullivan, 1978; Crabaugh and Kocurek, 1993), within the study area these thickness variations are minor, pre-date faulting, and do not impact the measured displacements. The horizons were chosen based on their continuity and ease of recognition along the 5 cliff faces, and to cover nearly the entire vertical extent of the cliff faces with a roughly even spacing between horizons. Horizon H1 corresponds to the top of the Dewey Bridge Member, which in the study area crops out at the base of each cliff face apart from cliff faces 1 and 5 (Fig. 4). Horizons H2 to H6 are all within the Slick Rock Member and can be mapped on all cliff faces. Horizons H2 to H5 correspond with mudstone layers up to tens of cm thick, while horizon H6 marks the transition from a red-orange sandstone layer to a lighter orange sandstone near the top of the Slick Rock Member (Fig. 4). Finally, H7 horizon corresponds to the boundary between the Slick Rock Member and the overlying Moab Tongue Member (Fig. 4).

Fault maps were initially prepared in the field from outcrop observations. Field mapping was particularly useful on the Moab Tongue platforms, where closely spaced joints (i.e., <1 m spacings) made it difficult to locate faults precisely from the VOM, for example, on the

rock pavement between cliff faces 3 and 4 (see Supplementary Figs. 2 and 3). Fault plane and slickenlines orientations were collected in the field at all accessible locations including the rock pavement between faces 3 and 4 and the lowermost 2–5 m of most of the cliff faces (faults measured on Face 2 are published in Camanni et al., 2023). Field mapping of faults was augmented and refined using the VOM, where faults could be identified directly, recognised from topographic changes in the rock pavements and variations in the strike of joints. Fault-surface orientations were extracted from the VOM in the area between faces 1 and 2.

3.2. Fault displacement analysis

The final step of the workflow required measurement of throw of the mapped horizons to estimate spatial throw variations on the two relay-bounding faults and subordinate faults. Fault throw was measured as the vertical distance between footwall and hangingwall cut-off lines on the fault surfaces of the 7 mapped horizons. Where the relay-bounding faults comprised more than one segment (see section 4.1), their throws were summed to simplify displacement analysis. Horizontal and vertical throw gradients were determined using the footwall and hangingwall cut-off lines of each horizon and for each of the five cliff faces, respectively (see Supplementary Fig. 4). These measurements were used to construct horizontal and vertical throw profiles.

4. Relay zone structure: map and cross-sections

A total of 88 faults were mapped in the region of the relay structure (Figs. 5–8). The two relay-bounding faults have the largest horizontal and vertical extents, and the largest throws. The relay-bounding faults are north-dipping and have a normal sense of slip. In addition to the main relay-bounding faults, there are two sets of normal faults, one antithetic (ca. south-dipping) and one synthetic (ca. north-dipping) to the main structures. These subordinate faults, which mainly have smaller throws and shorter lengths than the relay-bounding faults, are located within, or adjacent to, the relay zone. In the following sections, we describe all sets of faults with the aid of a structural map (Fig. 5), cross-sections through the interpreted VOM (Fig. 6), field photos at specific locations (Fig. 7), and a selection of the interpreted 3D fault surfaces (Fig. 8).

4.1. Relay-bounding faults

The relay-bounding hangingwall fault (the northern boundary of the relay zone) crosses the entire study area and crops out on all cliff faces and rock pavements with a total mapped length of ca. 1.3 km (Fig. 5). On Face 2, this fault comprises two fault splays that merge downwards into a single fault near the top of the Dewey Bridge Member (i.e., horizon H1; Fig. 6B and 7A). On Face 3, it comprises two segments with the footwall segment accommodating the largest throw and the hangingwall segment tipping out a few metres above horizon H7 (Figs. 5, 6C and 7B). The hangingwall relay-bounding fault is associated with a prominent step in the topography of the Moab Tongue Member on the rock pavement between faces 3 and 4 (Fig. 7C), where its throw is ca. 8 m (see later description of the throw distribution on this fault). Finally, on Face 5 the relay-bounding hangingwall fault comprises a tens of metres long fault-bound lens near the base of the cliff (Fig. 6E and 7D).

The relay-bounding footwall fault does not entirely cross the study area but crops out on faces 1 to 3 (Fig. 6A, B, C), tipping out on the rock pavement between faces 3 and 4, about 200 m west of Face 3 (Fig. 5). On Face 3, the fault splays upwards into two fault segments from near the top of the Dewey Bridge Member, with the footwall-most splay being further segmented at a smaller scale (Figs. 6C and 7E). These splays can be traced in map view on the rock pavement between faces 3 and 4 to the tip of the fault (Fig. 5).

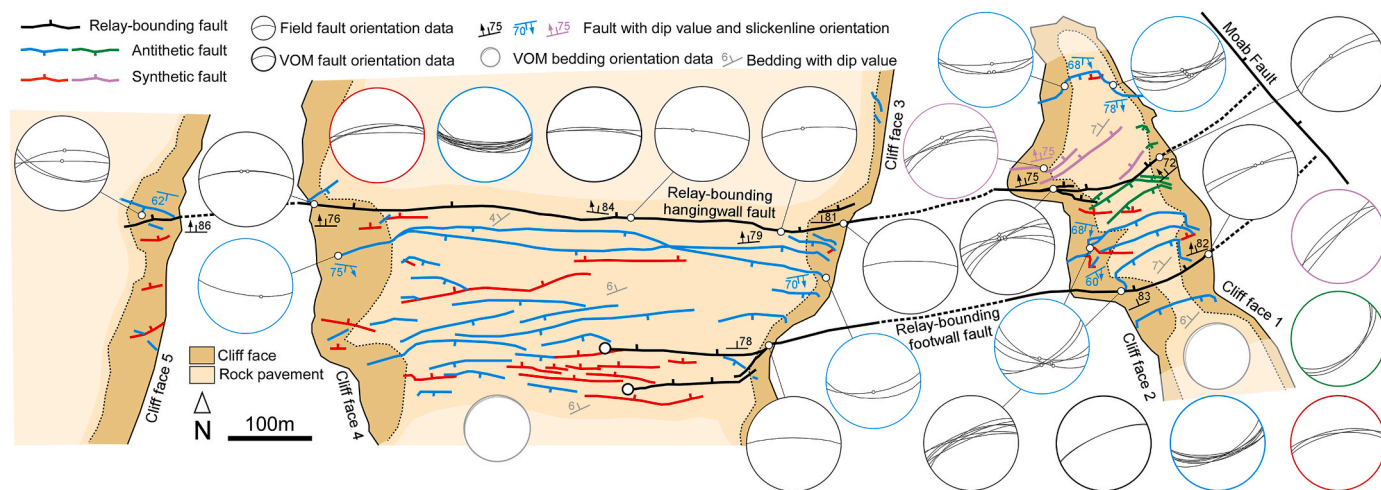Field and VOM measurements indicate that both relay-bounding

Fig. 5. Structural map of the faults mapped throughout the study area. In the plots are illustrated fault orientation data derived from (i) the 3D fault surfaces built within the VOM, and (ii) measurements collected directly in the field at the button of the cliff faces or on the rock pavement between faces 3 and 4. Where detectable, the latter include slip vectors recorded as slickenlines on the fault surfaces (dot on the faults in the plots indicate the trend and the plunge of the direction of movement of the downthrowning hangingwall fault block). Representative faults (with slickenlines where detected) are also directly shown in the map. Colours of the borders of the plots correspond to colours of the faults to which they refer. The blurred areas correspond to zones that were not mapped with the same level of detail as the rest of the study area, largely due to a lower resolution of the VOM there. (For interpretation of the references to colour in this figure legend, the reader is referred to the Web version of this article.)

faults roughly strike ENE-WSW on cliff faces 1 and 2, and bend to a more E-W orientation at about cliff Face 3 (see plots in Fig. 5). Both faults maintain this E-W orientation west of cliff Face 3 for the remainder of their mapped outcrop extent (Fig. 5). Slickenlines recorded on fault surfaces on both relay-bounding faults indicate dominantly normal dip-slip senses of movement throughout the study area (Fig. 5). However, minor slightly oblique slickenlines measurements (pitch ca. 70°) were also recorded on the hangingwall fault exposed on the rock pavement between faces 3 and 4, and on the footwall fault exposed on Face 1 (Fig. 5). These slightly oblique slickenlines may be associated with a late oblique reactivation of these faults as described in a previous study by van Gent and Urai (2020).

4.2. Antithetic faults

In total, 55 antithetic faults were mapped in the study area (blue and green faults in Figs. 5 and 6). These faults are mostly confined within the relay zone, as particularly apparent on cliff faces 1, 2, and 3 where both relay-bounding faults occur (see plots in Fig. 6 A, B, and C), and from the rock pavement between cliff faces 1 and 2 where the map area extends well-beyond the footwall and the hangingwall of the relay zone (Figs. 5 and 6). These antithetic faults are also abundant in the area on the rock pavement between faces 3 and 4, immediately west of the tip of the footwall relay-bounding fault (Figs. 5 and 6). This spatial association suggests that the antithetic faults are genetically related to the relay zone. Among the antithetic faults confined within the relay zone, several are exposed in cliff faces 1 and 2, and can be followed across the intervening rock pavement (blue faults in Figs. 5 and 6 A, B and Fig. 7F; see also blue fault surfaces in Fig. 8). These faults have maximum throws of up to 3.2 m (see section 5). Additional antithetic faults with significant vertical extents and maximum throws of up to ca. 2 m, can be mapped on faces 3 and 4 and on the rock pavement in between, where they can form hundred-meter-long fault-bound lenses (Fig. 5). In cross-section, the antithetic faults are commonly confined between and/or abut against relay-bounding faults displaying the geometry shown in Fig. 1C (Figs. 6 and 7).

Antithetic faults mainly strike sub-parallel to the relay-bounding faults and display the same change in strike from ca. ENE-WSW in cliff faces 1 and 2, and E-W west of Face 2 (Fig. 5). Exceptions to these orientations include six antithetic faults that are developed across the

hangingwall relay-bounding fault and are mapped (from fault surfaces built on the VOM) on cliff face 1 and tip out on Face 2 (green faults in Figs. 5, 6A and 8). These faults overall display an NE-SW orientation (Fig. 5). Slickenlines measured on all antithetic faults indicate both dip-slip and slightly oblique normal sense of movement (Fig. 5). Oblique slickenlines were measured on cliff face 2, at the hangingwall of the relay-bounding hangingwall fault and between the two relay-bounding faults, and on cliff face 4 at the footwall of the hangingwall fault (Fig. 5).

4.3. Synthetic faults

A total of 31 synthetic faults were mapped in the study area (red and pink faults in Figs. 5 and 6). These faults have shorter horizontal and vertical extents than the two relay-bounding faults, and are largely confined to either individual faces or to the rock pavement between faces 3 and 4. Synthetic faults cropping out between cliff faces 1 and 2 display the largest throws (ca. 1 m; Fig. 6A and B), and are either confined to the relay zone or located in the hangingwall of the relay-bounding hangingwall fault (respectively, red and pink faults in Figs. 5 and 6A, B). Synthetic faults within the relay zone strike sub-parallel to the relay-bounding faults (i.e., ENE-WSW to E-W), while those in the immediate hangingwall of the main fault have a NE-SW orientation (Fig. 5). However, at the base of cliff Face 2 one of the faults belonging to this second group rotates into a more ENE-WSW strike (Fig. 5). Between cliff faces 3 and 4, synthetic faults display small throws (i.e., tens of centimetres) and seem to only affect the Moab Member and the uppermost 2–3 m of the Slick Rock Member. In this area, most synthetic faults are clustered around the tip of the footwall relay-bounding fault and are sub-parallel to it (i.e., nearly E-W striking; Fig. 5). Slickenlines were recorded on only one synthetic fault at the bottom of Face 2 and display a pure dip-slip normal sense of movement (Fig. 5).

5. Fault throw profiles

Profiles of throw were constructed for the relay-bounding faults and the largest antithetic faults. The profiles are presented for individual horizons and cliff faces, which display horizontal and vertical throw variations, respectively. The shapes of the horizon throw profiles on individual relay-bounding faults are similar, although their throw
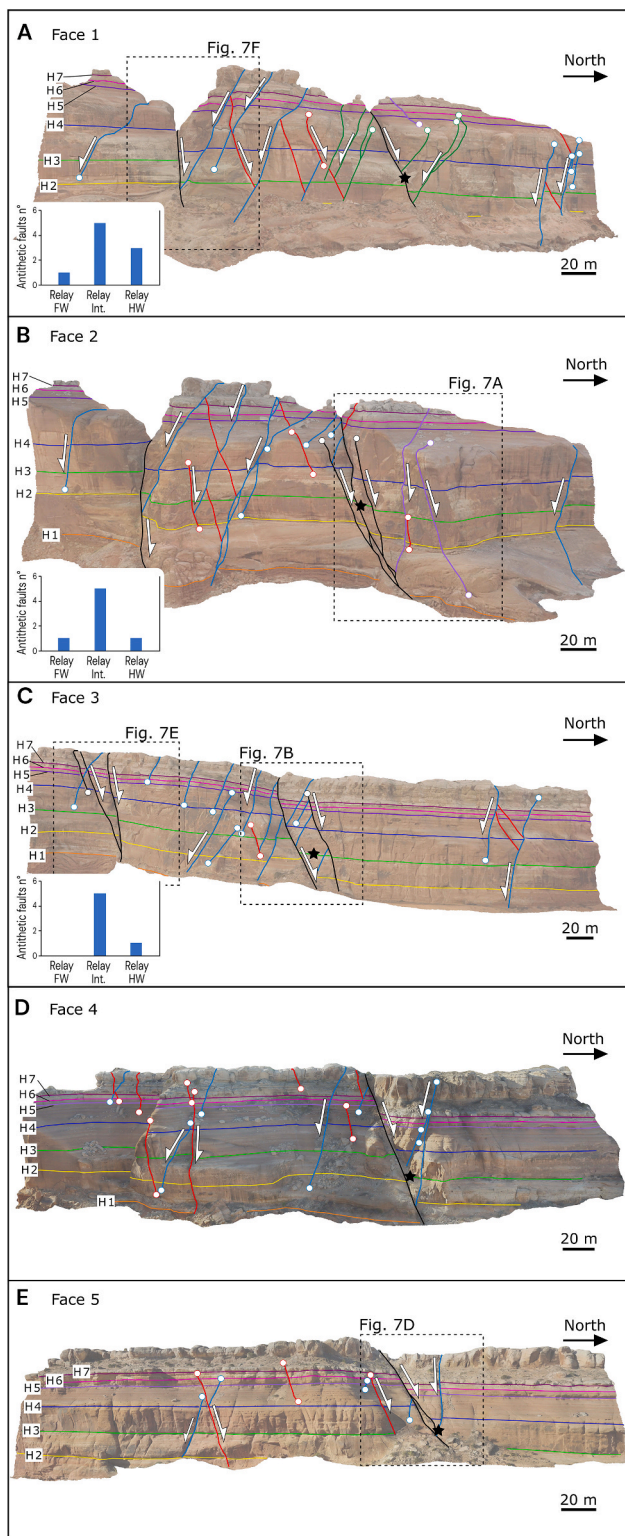
Fig. 6. Interpreted cliff faces (corresponding to vertical cross-sections through the study outcrop). The mapped horizons and faults are annotated. **A:** cliff Face 1; **B:** cliff Face 2 (horizontally flipped); **C:** cliff Face 3; **D:** cliff Face 4 (horizontally flipped): **E:** cliff Face 5. The plots in the bottom left corner of **A**, **B**, and **C** display the number of antithetic faults offsetting horizon H3 (located near the centre of the cliffs) in the footwall (FW), interior (int.), and hangingwall (HW) of the relay zone. Location of the cliff faces is indicated in Figs. 3 and 5. The cliff faces are rotated so that bedding is horizontal for ease of description, although bedding roughly dipping 4°–7° towards the NW-NNW in the study area. The black star on the hangingwall relay-bounding fault correspond to the intersection of a horizontal line lying on the fault surface with each section.

magnitudes vary vertically (see below). Here we describe only profiles for horizons accommodating the largest throws on each of the relay-bounding faults; these are Horizon 7 (the uppermost horizon) and Horizon 2 for the footwall and the hangingwall relay-bounding faults, respectively (Fig. 9A).

The relay-bounding footwall fault has a maximum throw of 12 m on cliff Face 1 that decreases to 8 m on Face 3 (see FW Fault Fig. 9A). The western tip of the fault is mapped on the rock pavement between faces 3 and 4. The tip point on horizon 7 is interpreted to be close to the mapped point as horizon 7 is only a few metres beneath the level of the rock pavement (Fig. 9A).

The throw on the relay-bounding, hangingwall fault increases westward (see HW Fault in Fig. 9A). Horizon 2 has a throw of ca. 5 m on Face 1 that increases to ca. 12 m on Face 4 (Fig. 9A) and decreases again on Face 5 (Fig. 9A). The profiles are similar for all horizons although there is some variability in the horizontal throw gradients of the stratigraphically lower horizons (i.e., H2 and H3) between faces 2 and 3 (Fig. 9A). Extrapolation of the fault to the east suggests that the fault tip-line would be encountered ca. 500 m to the east of Face 1. This is ca. 360 m greater than the distance to the Moab Fault (which is at ca. 140 m from the hangingwall fault on cliff Face 1), and so the hanging wall relay bounding fault is interpreted to intersect the Moab Fault (Fig. 5). The decrease in throw on the hangingwall fault from Face 5 to Face 4 is attributed to transfer of throw onto the fault that lies immediately to the north (Fig. 3).

Collectively, the data indicate that the westward decrease in throw on the footwall fault is mirrored by an equivalent westward increase in throw on the hangingwall fault of the relay structure. In addition, the cumulative throw for these two faults on cliff faces 1 to 3 is approximately constant at 16 m (Fig. 9A). These observations demonstrate the horizontal transfer of displacement between these two faults and support the view that the intervening volume populated with its many minor faults is a relay zone.

Vertical throw profiles on cliff faces 1–3 also display complementary throw variations on the hangingwall and footwall bounding faults, with an upward increase in throw on the footwall relay-bounding fault and an upward decrease in throw on the hangingwall fault (Fig. 9B). Throw gradients on the two faults are broadly similar with opposite signs (Fig. 9B). The equal and opposite throw gradients are consistent with down-dip transfer of throw between the footwall fault and the hangingwall fault. In addition, if the throw gradients on the footwall fault remain approximately constant, we can expect the lower tip-line of this fault to be about 250–350 m below the canyon floors. Conversely, if the throw gradients on the hangingwall fault also remain approximately constant we could expect the upper tip-line of this fault to be about 100–200 m above the rock pavements east of cliff Face 4. This is suggesting that the study area may be in the upper part of the relay zone.

Comparison of vertical and horizontal throw gradients indicates that, for both relay-bounding faults, the vertical throw gradients measured on cliff faces are consistently larger than the horizontal throw gradients on the mapped horizons (Fig. 9C). The average horizontal gradient of 0.007 is significantly lower than the average vertical gradient of 0.04 and the largest measured horizontal gradient (0.017 on Horizon 2 between Faces 1 and 2) is roughly equal to the lowest measured vertical throw gradient (hangingwall fault on Face 2). It is worth noting that the distance between throw measurements for the vertical profiles is significantly lower than that for the horizontal ones (i.e., the distance between cliff faces) and therefore, for the same throw variation between adjacent sample points, this will promote higher vertical than horizontal throw gradients. However, this cannot account for the difference in gradient between the two sampling directions as vertical throw gradients are here calculated for the envelope between the upper and the lower sample points on each cliff face. We conclude that the higher vertical throw gradients imply that the transfer of displacement is achieved over a shorter vertical than horizontal distance in this relay zone.

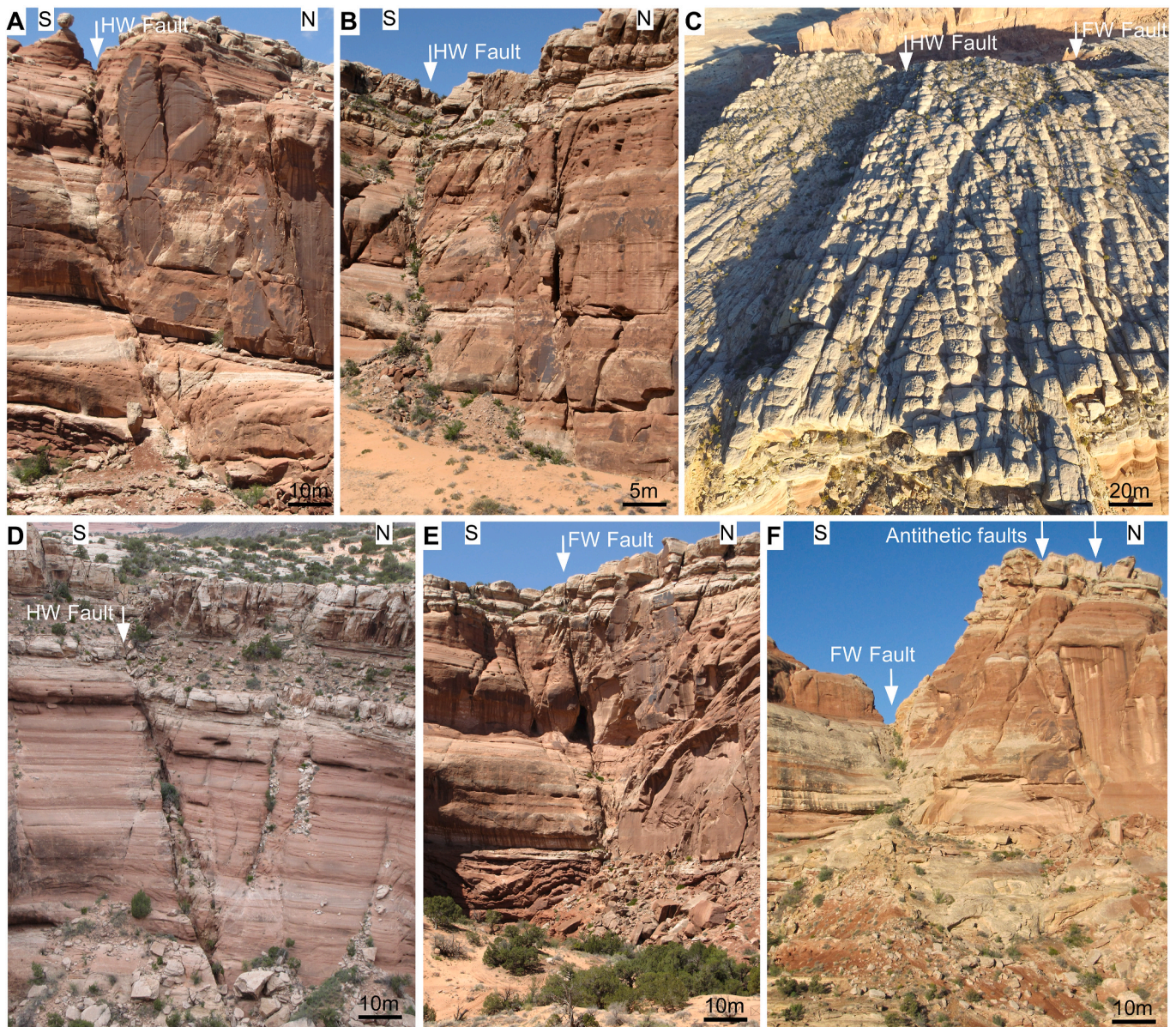Fig. 9B also includes the vertical throw profiles of 4 antithetic faults

Fig. 7. Field photos of selected locations within the study outcrop. HW Fault: relay-bounding hangingwall fault. FW Fault: relay-bounding footwall fault. Location of photos is indicated in Fig. 5. For details on the fault interpretation of each photo the reader is referred to Fig. 6. Note that **A** is horizontally flipped for consistency with Fig.6B.

mapped within the relay zone exposed on faces 1 and 2 (blue fault surfaces on the VOM in Fig. 8). All antithetic faults analysed here display constant throws of between 1.8 m and 3.2 m along their observed lengths. (Fig. 9B).

6. Discussion

Throw data for the relay-bounding faults display horizontally and vertically complementary variations in throw (Fig. 9). In detail, the throw on the footwall fault decreases eastward towards its tip and downwards, while the throw on the hangingwall fault decreases westwards and upwards. These patterns of throw distribution have been used to develop a 3D geometric model for the fault-segment boundaries, and suggests that, in map view, the relay-bounding faults have a right sense of stepping (Fig. 10A and B), while in cross-sectional view they form a contractional step (Fig. 10A, C).

The likely large-scale 3D structure of the relay zone may be further constrained by the relative magnitudes of the measured horizontal and vertical throw gradients. Throw gradients will be a maximum on a profile perpendicular to the tiplines of the faults bounding a relay zone, i.e., on a map of a neutral relay zone or on a cross-section through a dip relay zone, and nearly null in a direction parallel to the tiplines, i.e., a vertical section through a neutral relay zone or a horizontal slice through a dip relay zone. The finite throw gradients measured on the map and cross-section through the mapped relay zone imply that it is oblique, and the higher gradients seen on the vertical section imply that the relay zone is closer to a dip than map-view relay zone. The measured vertical gradients are generally 3 to 4 times larger than horizontal gradients consistent with a relay zone axis (here defined as the line normal to the direction of largest throw transfer, following Camanni et al., 2019) that plunges ca. 20° toward the east (Fig. 10D).

The likely extent of the relay zone bounding faults can be evaluated by extrapolating the measured throw profiles to locate the fault tip-points (yellow and blue stars on Fig. 10D) by assuming that throw gradients within the relay zone maintain a roughly constant magnitude, a condition most often observed in nature. The horizontal relay overlap
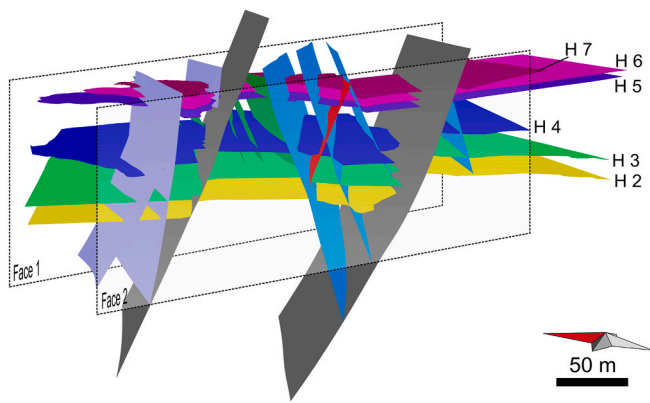
Fig. 8. Selected fault surfaces built on the VOM between cliff faces 1 and 2. H2 to H7 horizons are also displayed. The view is taken by looking into cliff Face 2 from West, in a perspective mode.

length, derived from the mapped tip of the footwall fault and the predicted location of the tip of the hangingwall fault (Fig. 9A) is ca. 1300 m, although it may be curtailed slightly if the hangingwall fault extends to intersect the Moab Fault. The predicted elevations of the lower tip of the footwall fault and the upper tip of the hangingwall fault indicate a vertical overlap of between ca. 450 m and 650 m (Fig. 10D). The estimated upper tipline of the hangingwall fault is approximately horizontal while the lower tip of the footwall fault, constrained by the tip-point seen on map view and vertical throw profiles derived from 3 cliff sections plunges towards the east.

An important question remains about how the displacement variations across the relay-bounding faults are achieved. Horizon geometries, along with changes in throw, suggest that horizontal transfer of displacement is achieved through the development of an east-dipping relay ramp at all mapped horizons (Figs. 11 and 12), in the same fashion as "neutral" relay zones (Peacock and Sanderson, 1991, 1994; Cartwright et al., 1996; Crider and Pollard, 1998; Peacock, 2002; Fossen and Rotevatn, 2016; Camanni et al., 2019; see Fig. 1A). However, because the horizontal dimension of the relay zone is large (~1300 m) and the displacements of the relay-bounding faults small (<12 m) the beds rotations in the relay zone accommodating horizontal transfer of displacement are <1° (ca. 0.5°). While these rotations are too small to be directly observed in bedding measurements the presence of the ramp is apparent from the mapped horizon surfaces (Fig. 11; note that in the figure there is a vertical exaggeration of four times).

How displacement is transferred vertically within the relay zone is less clear. Two main mechanisms of vertical displacement transfer have been proposed for contractional, dip relay zones: contractional volumetric strains and antithetic faulting (Peacock and Zhang 1993; Childs et al., 1996, 2009; Rykkelid and Fossen, 2002; van der Zee and Urai, 2005; Camanni et al., 2019, 2023, Fig. 1B and C). Fault mapping in this study indicates two sets of subordinate faults that strike sub-parallel to the relay-bounding faults, one synthetic and one antithetic to the main faults (Fig. 5). The antithetic faults have the larger dimensions and throws and dominate the internal structure of the relay zone (Figs. 5 and 6) suggesting that they play an important role in the relay zone. Camanni et al. (2023) have recently shown that the antithetic-fault mechanism of vertical throw transfer is associated with bounding faults (i.e., R shears, according to the authors) that exhibit stepped throw profiles, with each step occurring across branchpoints with abutting antithetic faults (i.e., R′ shears; see Fig. 1C). Additionally, they also demonstrated that R' shears function as throw conveyors, maintaining nearly constant throw along their vertical length, with a throw magnitude similar to that of the steps in throw observed on the bounding R shear(s) at the branchpoint where they intersect (see Camanni et al., 2023). The resolution of the data used for mapping displacement in the present study (i.e., the number of layers that can be mapped) is not
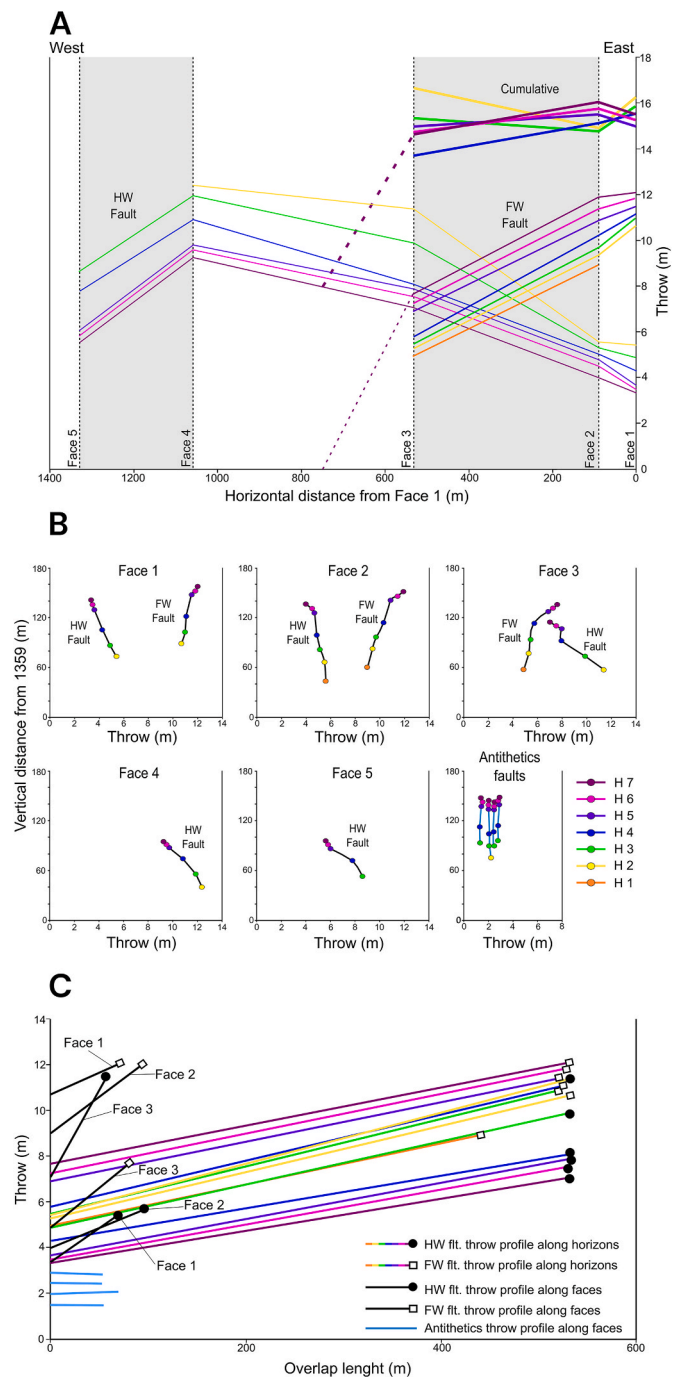

Fig. 9. Displacement data of the studied faults. **A:** horizontal throw profiles for the relay-bounding faults; **B:** vertical throw profiles for the relay-bounding faults and selected antithetic faults within the relay zone on faces 1 and 2 (see Fig. 8); **C:** comparison between horizontal and vertical throw profiles of the relay-bounding faults and the selected antithetic faults (all at the same scale). Note that the ca. 530 length of the horizontal throw profiles in **C** correspond to the portions of the horizontal throw profiles measured between faces 1 and 3 in **A**.

sufficient to detect steps on the throw profile of the relay-bounding faults, however, throw profiles for the largest antithetic faults have near constant throws along their mappable vertical lengths (Fig. 9B), in agreement with the model of Camanni et al. (2023). Therefore, we propose that these antithetic faults deforming the relay ramp accommodate vertical transfer of displacement across the relay and between the relay-bounding faults (Fig. 12).
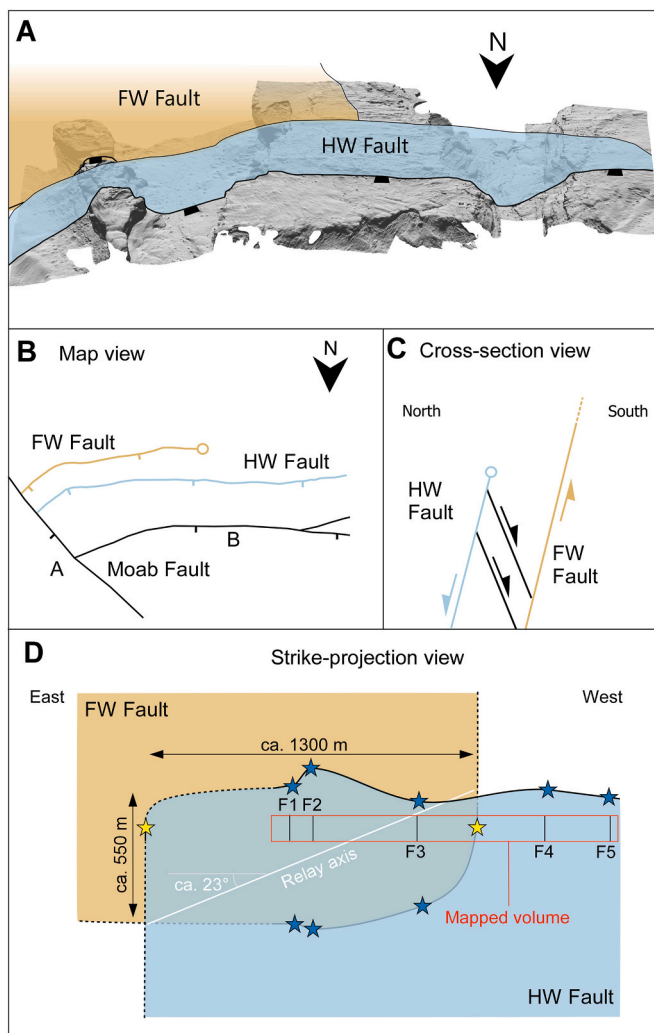
Fig. 10. 3D (**A**) and 2D (**B, C, D**) geometrical configuration of the relay-bounding faults as derived from structural and displacement analyses performed in this work. Scale is not the same in **A, B, C, D**. The relay-bounding faults have, in map view (**B**), a right sense of stepping and bound a neutral relay zone, while in cross-section (**C**) the relay zone is as a dip, contractional one. In strike projection view (**D**), the relay zone is oblique and dip of ca. 23° towards the East. Note that for simplicity the intersection of the relay zone with the Moab Fault is not considered in **D**. In **D**, the blue and yellow stars correspond to the points of null throw on the vertical and lateral throw profiles, respectively, after throw gradient extrapolations used for constraining the location of the relay zone tip lines. These extrapolations assume roughly constant throw gradients on the faults bounding the relay zone. (For interpretation of the references to colour in this figure legend, the reader is referred to the Web version of this article.)

Furthermore, comparison between the thickness of layers within and outside the relay zone (see Supplementary Fig. 5) does not indicate that within the relay zone layers are thinner than outside of it, further corroborating the antithetic faults model of vertical throw transfer, while making the contractional volumetric strains model unlikely. Why the vertical component of displacement transfer is accommodated via antithetic faults rather than by volumetric strains requires further investigation. A viable explanation for this is that the faulted massive quartz-rich sandstones do not readily accommodate volumetric strains, and this may promote the formation of antithetic faults instead. However, similar modes of displacement transfer have been recognised in very weak rocks with very high porosities (see, e.g., Camanni et al., 2023 and references therein), so that lithology cannot be assumed to be a general explanation for the occurrence of antithetic faulting rather than
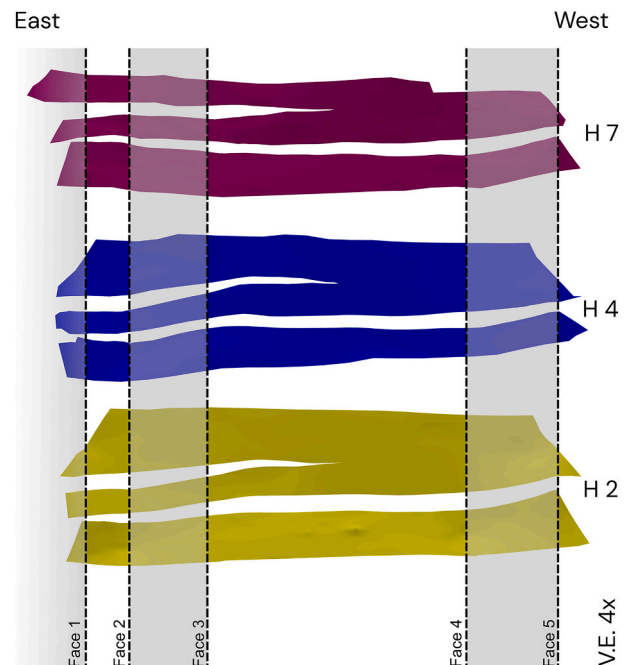

Fig. 11. Horizontal transfer of displacement between the relay-bounding fault segments accommodated by relay ramp geometries at several overlying horizons. As a selection, in the figure, east-dipping relay ramps at horizons H2, H4, and H7 are displayed, although the same geometry can also be recognised on the other horizons. The tip of the footwall fault is approximated to coincide with the tip of the fault as mapped on the Moab Tongue Member on the rock pavement by assuming a roughly vertical tip line between H7 and H2. Note that the figure is vertically exaggerated four times, and the view is taken by looking from North in a perspective mode.

volume loss in contractional relay zones.

The results of this work provide insights on the possibility to extrapolate 3D geometry from 2D observations carried out, for example, on outcrop or seismic reflection data. When antithetic faults are associated with a relay zone detected in cross-sections with a Riedel-like geometry, one should expect that a relay ramp exists within the plane of inspection (Fig. 12). Similarly, antithetic faults internally deforming a ramp seen in map-view may suggest a contractional relay zone geometry within the plane of inspection (Fig. 12). These could be used for predicting the 3D geometry and internal structure of relay zones from 2D observations. These predictions can be of significance for a range of industry applications that involve faults and associated fluid flow in the subsurface such as CO_2 and H_2 storage, geothermal and hydrocarbon exploration and production, and mining and civil engineering.

7. Conclusions

We have mapped and analysed the 3D geometry and displacement of a reservoir-scale relay zone cropping out adjacent to the Moab Fault at Courthouse Rock (Utah, USA). We conclude that:

1. The relay zone has a complex internal structure associated with two sets of subordinate faults, one synthetic and one antithetic to the relay-bounding faults - the latter made up of faults with larger throws and extents than the former;
2. The relay-bounding faults are associated with maximum throw of ca. 12 m which vary both horizontally and vertically. These throw variations indicate that, in map view, the relay-bounding faults have a right sense of stepping, while in cross-sectional view they form a contractional step, defining in 3D an oblique relay zone;
3. This geometrical arrangement requires displacement to be transferred both horizontally and vertically across the study relay zone.
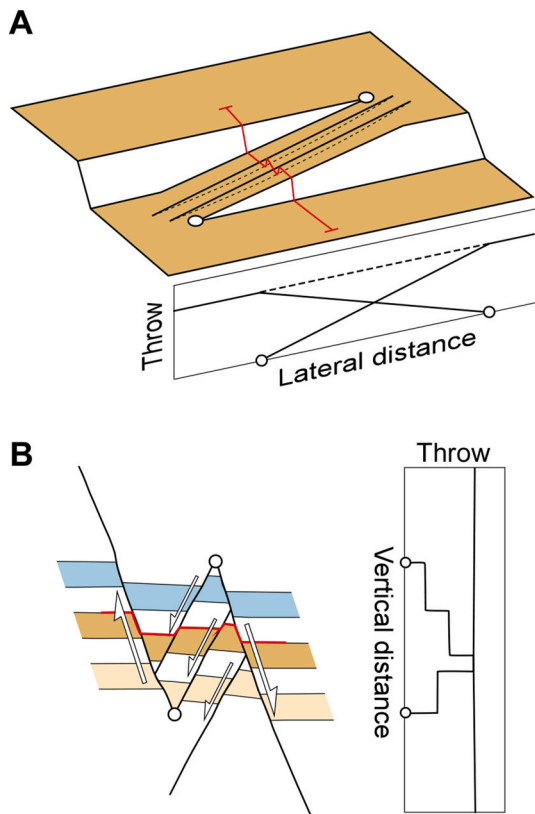
Fig. 12. Mechanisms for transferring displacement horizontally (**A**) and vertically (**B**) across the same relay zone: relay ramp, and antithetic faulting, respectively. **A**: Oblique view of relay ramp on faulted horizon (brown polygon). Plot beneath the horizon shows fault throw profiles for individual faults (solid lines) and the total throw (dashed line). Red line indicates the location of the cross section in **B**. **B**: Cross section showing primary relay-forming faults, secondary antithetic faults, and displaced horizons. Mapped horizon in **A** is shown in red. Vertical throw profile for the primary relay faults in also shown (right). (For interpretation of the references to colour in this figure legend, the reader is referred to the Web version of this article.)

Horizontal transfer of displacement is accommodated by the development of a relay ramp, while vertical displacement transfer is facilitated by antithetic faulting primarily within the ramp

4. These results suggest that multiple mechanisms can work in conjunction to transfer displacement across individual relay zones, and that the structure of the relay zone departs from the "neutral" and "dip" relay zone end-members.

CRediT authorship contribution statement

Giovanni Camanni: Conceptualization, Data curation, Formal analysis, Supervision, Investigation, Methodology, Writing – original draft. **Giovanni Freda:** Conceptualization, Data curation, Formal analysis, Investigation, Visualization, Methodology, Writing – review & editing. **Efstratios Delogkos:** Conceptualization, Investigation, Methodology, Writing – review & editing. **Andrew Nicol:** Investigation, Methodology, Writing – review & editing. **Conrad Childs:** Conceptualization, Investigation, Methodology, Supervision, Funding acquisition, Project administration, Writing – review & editing.

Declaration of competing interest

The authors declare that they have no known competing financial interests or personal relationships that could have appeared to influence the work reported in this paper.

Data availability

Data will be made available on request.

Appendix A. Supplementary data

Supplementary data to this article can be found online at https://doi.org/10.1016/j.jsg.2023.105001.

References

Camanni, G., Roche, V., Childs, C., Manzocchi, T., Walsh, J., Conneally, J., Saqab, M.M., Delogkos, E., 2019. The three-dimensional geometry of relay zones within segmented normal faults. J. Struct. Geol. 129, 103895.

Camanni, G., Vinci, F., Tavani, S., Ferrandino, V., Mazzoli, S., Corradetti, A., Parente, M., Iannace, A., 2021. Fracture density variations within a reservoir-scale normal fault zone: a case study from shallow-water carbonates of southern Italy. J. Struct. Geol. 151.

Camanni, G., Childs, C., Delogkos, E., Roche, V., Manzocchi, T., Walsh, J., 2023. The role of antithetic faults in transferring displacement across contractional relay zones on normal faults. J. Struct. Geol.

Cartwright, J.A., Mansfield, C., Trudgil, B., 1996. The growth of normal faults by segment linkage. Geol. Soc., London, Special Publ. 99, 163–177.

Childs, C., Watterson, J., Walsh, J.J., 1995. Fault overlap zones within developing normal fault systems. J. Geol. Soc. 152, 535–549.

Childs, C., Nicol, A., Walsh, J.J., Watterson, J., 1996. Growth of vertically segmented normal faults. J. Struct. Geol. 18, 1389–1397.

Childs, C., Manzocchi, T., Walsh, J.J., Bonson, C.G., Nicol, A., Schöpfer, M.P.J., 2009. A geometric model of fault zone and fault rock thickness variations. J. Struct. Geol. 31, 117–127.

Crabaugh, M., Kocurek, G., 1993. Entrada Sandstone: an Example of a Wet Aeolian System, vol. 72. Geological Society, London, Special Publications, pp. 103–126.

Crider, J.G., Pollard, D.D., 1998. Fault linkage: three-dimensional mechanical interaction between echelon normal faults. J. Geophys. Res. Solid Earth 103, 24373–24391.

Davatzes, N.C., Aydin, A., Eichhubl, P., 2003. Overprinting faulting mechanisms during the development of multiple fault sets in sandstone, Chimney Rock fault array, Utah, USA. Tectonophysics 363 (1–2), 1–18.

Davatzes, N., C, Eichhubl, P., Aydin, A., 2005. Structural evolution of fault zones in sandstone by multiple deformation mechanisms: Moab fault, southeast Utah. GSA Bullet. 117 (1–2), 135–148.

Delogkos, E., Manzocchi, T., Childs, C., Sachanidis, C., Barbas, T., Schöpfer, M.P., Chatzipetros, A., Pavlides, S., Walsh, J.J., 2017. Throw partitioning across normal fault zones in the Ptolemais Basin, Greece. In: Childs, C., Holdsworth, R.E., Jackson, C.A.-L., Manzocchi, T., Walsh, J.J., Yielding, G. (Eds.), The Geometry and Growth of Normal Faults, vol. 439. Geological Society of London, Special Publication.

Delogkos, E., Manzocchi, T., Childs, C., Camanni, G., Roche, V., 2020. The 3D structure of a normal fault from multiple outcrop observations. J. Struct. Geol. 136.

Doelling, H.H., 1985. Geology of arches national park. Utah Geol. Mineral Survey Map 74, 2 scale 1:50,000.000.

Doelling, H.H., 1988. Geology of salt valley anticline and arches national park, Grand County Utah. In: Salt Deformation in the Paradox Region, Utah Geological and Mineral Survey Bulletin, vol. 122, pp. 1–60.

Doelling, H.H., 2001. Geologic map of the Moab and eastern part of the san rafael desert 30' x 60' quadrangles, grand and emery Counties, Utah, and Mesa County, Colorado. Utah Geological Survey Map 180 scale 1:100,000.

Ferrill, D.A., McGinnis, R.N., Morris, A.P., Smart, K.J., Sickmann, Z.T., Bentz, M., Lehrmann, D., Evans, M.A., 2014. Control of mechanical stratigraphy on bed-

restricted jointing and normal faulting: eagle Ford Formation, south-central Texas. American Assoc. Petroleum Geol. Bullet. 98 (11), 2477–2506.

Fossen, H., Rotevatn, A., 2016. Fault linkage and relay structures in extensional settings—a review. Earth Sci. Rev. 154, 14–28.

Foxford, K.A., Garden, I.R., Guscott, S.C., Burley, S.D., Lewis, J.L.L., Walsh, J.J., Watterson, J., 1996. The field geology of the Moab Fault. In: Huffmann, A.C., Lund, W.R., Godwin, L.H. (Eds.), Geology and Resources of the Paradox Basin. Utah Geological Association Guidebook, pp. 265–283.

Foxford, K.A., Walsh, J.J., Watterson, J., 1998. Structure and content of the Moab Fault Zone, Utah, USA, and its implications for fault seal prediction. In: Jones, G., Fisher, Q.J., Knipe, R.J. (Eds.), Faulting Fault Sealing and Fluid Flow in Hydrocarbon Reservoirs, vol. 147. Geological Society, London, Special Publications, pp. 87–103.

Huggins, P., Watterson, J., Walsh, J.J., Childs, C., 1995. Relay zone geometry and displacement transfer between normal faults recorded in coal-mine plans. J. Struct. Geol. 17, 1741–1755.

Johansen, T., S, E., Fossen, H., Kluge, R., 2005. The impact of syn-faulting porosity reduction on damage zone architecture in porous sandstone: an outcrop example from the Moab Fault, Utah. J. Struct. Geol. 27, 1469–1485.

Kristensen, M.B., Childs, C.J., Korstgård, J.A., 2008. The 3D geometry of small-scale relay zones between normal faults in soft sediments. J. Struct. Geol. 30, 257–272.

Maerten, L., 2000. Variation in slip on intersecting normal faults: implications for paleostress inversion. J. Geophys. Res. 105 (25), 553-525, 565.

Marchal, D., Guiraud, M., Rives, T., 2003. Geometric and morphologic evolution of normal fault planes and traces from 2D to 4D data. J. Struct. Geol. 25, 135–158.

McKnight, E.T., 1940. Geology of Area between Green and Colorado Rivers, Gran and San Juan Counties, vol. 232. Utah Geological Survey Open-File Report.

Mercuri, M., McCaffrey, K.J.W., Smeraglia, L., Mazzanti, P., Collettini, C., Carminati, E., 2020a. Complex geometry and kinematics of subsidiary faults within a carbonate-hosted relay ramp. J. Struct. Geol. 130.

Mercuri, M., Carminati, E., Tartarello, M.C., Brandano, M., Mazzanti, P., Brunetti, A., McCaffrey, K.J.W., Collettini, C., 2020b. Lithological and structural control on fracture frequency distribution within a carbonate-hosted relay ramp. J. Struct. Geol. 137.

Nicol, A., Walsh, J.J., Childs, C., Manzocchi, T., 2020. The growth of faults. In: Tanner, D., Brandes, C. (Eds.), Understanding Faults: Detecting, Dating, and Modeling. Elsevier.

Nuccio, V.F., Condon, S.M., 1996. Burial and Thermal History of the Paradox Basin, Utah and Colorado, and Petroleum Potential of the Middle Pennsylvanian Paradox Basin. US Geological Survey, Reston, VA, USA.

Peacock, D.C.P., Sanderson, D.J., 1991. Displacements, segment linkage and relay ramps in normal fault zones. J. Struct. Geol. 13 (6), 721–733.

Peacock, D.C.P., Zhang, X., 1993. Field examples and numerical modelling of oversteps and bends along normal faults in cross-section. Tectonophysics 234, 147–167.

Peacock, D.C.P., Sanderson, D.J., 1994. Geometry and development of relay ramps in normal fault systems. AAPG (Am. Assoc. Pet. Geol.) Bull. 78, 147–165.

Peacock, D.C.P., 2002. Propagation, interaction and linkage in normal fault systems. Earth Sci. Rev. 58, 121–142.

Pipiringos, G.S., O'Sullivan, R.B., 1978. Principal Unconformities in Triassic and Jurassic Rocks, Western Interior United States – A Preliminary Study. U.S. Geological Survey Professional Paper, p. 29. https://doi.org/10.3133/pp1035A, 1035-A.

Putz-Perrier, M.W., Sanderson, D.J., 2008. Spatial distribution of brittle strain in layered sequences. J. Struct. Geol. 30, 50–64.

Roche, V., Childs, C., Madritsch, H., Camanni, G., 2020. Layering and structural inheritance controls on fault zone structure in three dimensions: a case study from the northern Molasse Basin, Switzerland. J. Geol. Soc.

Roche, V., Camanni, G., Delogkos, E., Childs, C., Manzocchi, T., Walsh, J., Conneally, J., Saqab, M., Delogkos, E., 2021. Variability in the three-dimensional geometry of segmented normal fault surfaces. Earth Sci. Rev.

Rykkelid, E., Fossen, H., 2002. Layer rotation around vertical fault overlap zones: observations from seismic data, field examples, and physical experiments. Mar. Petrol. Geol. 19, 181–192.

Stokes, W.L., 1987. Geology of Utah. Utah geological and mineral survey. Occas. Pap. 6, 280.

Van der Zee, W., Urai, J.L., 2005. Processes of normal fault evolution in a siliciclastic sequence: a case study from Miri, Sarawak, Malaysia. J. Struct. Geol. 27, 2281–2300. https://doi.org/10.1016/j.jsg.2005.07.006.

van Gent, H., Urai, J.L., 2020. Abutting faults: a case study of the evolution of strain at Courthouse branch point, Moab Fault, Utah. Solid Earth 11 (Issue 2), 513–526.

Walsh, J.J., Watterson, J., 1989. Displacement gradients on fault surfaces. J. Struct. Geol. 11, 307–316.

Walsh, J.J., Bailey, W.R., Childs, C., Nicol, A., Bonson, C.G., 2003. Formation of segmented normal faults: a 3-D perspective. J. Struct. Geol. 25, 1251–1262.

Westoby, M.J., Brasington, J., Glasser, N.F., Hambrey, M.J., Reynolds, J.M., 2012. "Structure-from-Motion" photogrammetry: a low-cost, effective tool for geoscience applications. Geomorphology 179, 300–314.